CO_2 high-resolution simulation using WRF-GHG over the Kanto region in Japan

Jagat S. H. Bisht[1]*, Prabir K. Patra[1,2], Masayuki Takigawa[1], Yugo Kanaya[1], Masahiro Yamaguchi[1], Toshinobu Machida[3], and Hiroshi Tanimoto[3]

[1]Research Institute for Global Change, JAMSTEC, Yokohama, 236-0001, Japan

[2]Research Institute for Humanity and Nature, Kyoto, 603-8047, Japan

[3]Earth System Division, National Institute for Environmental Studies, Tsukuba, 305-8506, Japan

*corresponding author's e-mail: jagatbisht@jamstec.go.jp

Abstract

A high-resolution simulation of CO_2 at 1×1 km horizontal resolution using the Weather Research and Forecasting Greenhouse gas (WRF-GHG) model was conducted, focusing on the Kanto region in Japan. The WRF-GHG simulations were performed using different anthropogenic emission inventories: EAGrid (Japan, 1 km), EDGAR (0.1°), and EDGAR-downscaled (0.01°). Our analysis showed that the simulations using EAGrid better captured the diurnal variability in observed CO_2 compared to EDGAR and EDGAR-downscaled emissions at two continuous monitoring sites. The 1×1 km simulation performed better in simulating CO_2 variability observed in surface sites (hourly) and aircraft observations, compared to the 27×27 km simulations. We compared the vertical profile distribution of CO_2 and found that all the simulations performed similarly. During February (May), the anthropogenic (land biosphere) fluxes were the primary contributor to the vertical distribution of CO_2 up to an altitude of 3200 m (4500 m), beyond which long-range transport influenced by lateral boundary conditions from Eurasia played a greater role. The sensitivity analysis of boundary conditions showed a systematic bias (~ 4 ppm) persisting above 3200 m altitude when fixed (a constant value) boundary conditions are applied, as compared to the simulation with boundary conditions from a global model. We also compared the WRF-GHG simulated column-averaged XCO_2 from Orbiting Carbon Observatory-2 (OCO-2) satellite and found a statistically significant spatial correlation (r=0.47) in February. However, we found a weaker spatial correlation (0.17) in May, which could be caused due to under-representation of intense land biosphere activity in WRF-GHG.

Plain Language Summary

We performed high-resolution (1×1 km grid in horizontal) simulation of CO_2 over the Kanto region, Japan using a regional model (WRF-GHG) in order to better account for the small-scale processes. We used three different anthropogenic emission inventories for model simulations and evaluated their effectiveness by comparing the simulation results with surface-based, aircraft and satellite remote sensing observations. The high-resolution simulation better captures the CO_2 variability observed in surface and aircraft observations compared to coarser (27×27 km) spatial resolution. The vertical profile distribution of CO_2 aircraft observations is explained by different CO_2 tracers, for e.g., anthropogenic, land biosphere, biomass burning and ocean fluxes, and a background tracer from global transport model. Primary contributor to the vertical distribution of CO_2 is anthropogenic during February (up to 3200 m altitude) and land biosphere during May (up to 4500 m altitude), beyond which CO_2 is influenced by the background tracer from Eurasia. Without the lateral boundary conditions from global model a systematic bias could persist in CO_2 vertical profile from mid-troposphere. We compared WRF-GHG simulated column-averaged CO_2 concentration (XCO_2) with satellite observations, and found a much better spatial correlation for February compared to that for May.

Key Points

(1) The WRF-GHG model simulations are performed over Kanto region, Japan using three different anthropogenic emission inventories.

(2) WRF-GHG simulations are shown to be sensitive to lateral boundaries above middle troposphere based on comparison with aircraft observations.

(3) WRF-GHG at finer spatial resolution (1 km) performs better than the coarser (27 km) simulation when compared using in-situ observations.

1. Introduction

CO_2 is a well-mixed and long-lived greenhouse gas (GHG) in the atmosphere which has both anthropogenic and natural sources. CO_2 is chemically inert in the troposphere and stratosphere. CO_2 concentration is increasing steadily in the atmosphere because emissions by anthropogenic activity (10.9 ± 0.8 $GtCyr^{-1}$ for the year 2021) which far exceeds the uptakes from terrestrial ecosystem (3.5 ± 0.9 $GtC\ yr^{-1}$) and ocean (2.9 ± 0.4 $GtC\ yr^{-1}$), respectively (Friedlingstein et al., 2022). The attribution of CO_2 to its anthropogenic and natural flux components is a necessary step to understand the role of human-induced climate change.

To estimate gridded CO_2 emissions from various sources, such as industrial, residential, commercial,

and transportation processes, anthropogenic CO_2 emission inventories have been developed and are regularly updated and improved for better accuracy (Gurney et al., 2020; Janssens-Maenhout et al., 2019; Fukui et al., 2014). Model simulations using different emission inventories can help assess the performance of these inventories with respect to observed in-situ CO_2 concentration observations at local scale (Liu et al., 2015). Several studies have demonstrated that the current concentration of CO_2 in the atmosphere is largely due to human activities, particularly the burning of fossil fuels (Friedlingstein et al., 2022). It has been reported that more than 60% of global fossil-fuel CO_2 emissions are produced in cities (Duren and Miller, 2012; Huo et al., 2022), making them important targets for mitigation efforts.

In addition to anthropogenic CO_2 emissions, atmosphere-biosphere carbon exchange significantly affects the atmospheric CO_2 concentration and is equally important to understand the atmospheric carbon cycle. Numerous studies use top-down approach to understand the effect of all emissions of CO_2. In such approach various types of atmospheric inversion methods are used that uses CO_2 concentrations measurements and atmospheric transport models to estimate CO_2 flux. Inversions can produce estimates on a daily or sub-daily timescale, but regional assessments of fluxes using global models at small time and space scales are challenging due to transport model's inability to represent CO_2 measurements adjacent to large point sources (Pisso et al., 2019). However, efforts have been made to better parameterize the biosphere processes (Dayalu et al., 2018) and regional scale atmospheric inversion methods have been developed to estimate CO_2 fluxes (Steinkamp et al., 2017; Lauvaux et al., 2016).

Regional models are used for addressing the knowledge gap related to the mesoscale scale transport of carbon dioxide (CO_2) and its flux exchange between the biosphere and the atmosphere (Ballav et al., 2012; Ballav et al., 2016). Ahmadov et al. (2007, 2009) coupled Vegetation Photosynthesis and Respiration Model (VPRM) (Mahadevan et al., 2008) module with the WRF model, and conducted CO_2 modeling over Europe. This framework has also been utilized in other studies (Park et al., 2018; Dong et al., 2021; Pillai et al., 2016), which have demonstrated the effectiveness of the atmosphere-biosphere coupled model in capturing mesoscale CO_2 transport at regional and local scales with significant improvements. VPRM CO_2 fluxes are required to be fine-tuned using observed vegetation fluxes for the land use types in the region (Mahadevan et al., 2008).

This study is performed to evaluate the performance of WRF-GHG over Japan, specifically the Kanto region, centered around Tokyo, using three different anthropogenic emission inventories (EAGrid, EDGAR, and EDGAR-downscaled). Our WRF-GHG simulations efforts anticipates the launch of GOSAT-GW/TANSO-3 (Global Observing SATellite for Greenhouse gases and Water cycle/ Total Anthropogenic and Natural emissions mapping SpectrOmeter-3; scheduled to be launched in the fiscal year 2024-25) for XCO_2 observations. XCO_2 gives the information of whole atmospheric

column; therefore, the accuracy of the model will be assessed by comparing its results to surface and aircraft measurements of CO_2 concentrations, as well as XCO_2 observations from satellite. We chose two different months for the WRF-GHG simulation experiments: February and May, for mimicking two contrasting periods of dormant and intense land biosphere activity (e.g., Tohjima et al., 2020).

2. Materials and Methods

2.1 WRF-GHG Model configurations

We use WRF with coupled chemistry (WRF-Chem version 4.2.1) model, which uses the GHG module to simulate the transport of CO_2, methane (CH_4), and carbon monoxide (CO) (hereafter referred as WRF-GHG). The module includes VPRM to simulate the CO_2 biogenic emissions (described by Ahmadov et al., 2007 and Mahadevan et al., 2008). We run WRF-GHG for the following CO_2 tracers: background, biomass burning, ocean, biogenic, and anthropogenic. And the CO_2 concentration is estimated as the net total of them. The WRF-GHG simulations performed using two-moment microphysics (Morrison et al., 2009), Unified Noah Land Surface Model (Tewari et al., 2004), Grell 3D Ensemble (GD) (Grell and Dévényi, 2002) cumulus parameterization for outermost domain (d01; Fig.1), and the Rapid Radiative Transfer Model for GCMs (RRTMG) short and longwave radiation schemes. For Planetary Boundary Layer (PBL) parameterization, the MYNN (Mellor-Yamada-Nakanishi-Niino) 2.5 level Turbulent Kinetic Energy (TKE) based PBL scheme (Nakanishi and Niino, 2004) is used.

We set up and run WRF-GHG by two-way nesting at 27, 9, 3, and 1 km resolution on four nested domains (Fig. 1a) and 41 vertical layers extending up to 155 hPa. Initial and lateral boundary conditions for meteorological fields for the WRF-GHG modeling were taken from the European Centre for Medium-Range Weather Forecasts (ECMWF) Reanalysis (ERA-5) dataset which is available at 0.25^o spatial resolution. The CO_2 initial and lateral boundary conditions are provided from Model for Interdisciplinary Research on Climate, version 4.0 (MIROC4) based ACTM (hereafter referred to as MIROC4-ACTM) model output (spatial resolution is 2.8^o; Patra et al., 2018; Bisht et al., 2021). The model was spun up for 15 days prior to comparing it with the observations. The VPRM module in WRF-GHG model calculates the NEE based on NPP (Net Primary Productivity) and RESP (respiration rate) as follows:

$$\text{NEE} = \text{-NPP (Net Primary Productivity)} + \text{RESP (respiration rate)} \quad (1)$$

$$\text{NPP} = \lambda \times T_{scale} \times W_{scale} \times P_{scale} \times \frac{1}{(1 + PAR/PAR_0)} \times PAR \times EVI \quad (2)$$

$$\text{RESP} = \alpha \times T + \beta \quad (3)$$

The Enhanced Vegetation Index (EVI) and Land Surface Water Index (LSWI) calculated from the MODIS surface reflectance data are used to generate the scaling factors for temperature (T_{scale}), phenology (P_{scale}), and canopy water content (W_{scale}). These scaling factors and the VPRM parameters, including the maximum quantum yield (λ) and the half-saturation value of photosynthetically active radiation (PAR_0), are used to calculate the NPP. α and β are parameters used to model ecosystem respiration.

2.2 Emission Inventories

The WRF-GHG simulations have been performed over Japan using three different anthropogenic emission inventories: East Asian Air Pollutant Emission Grid Database (EAGrid) (Japan, 1 km), Emissions Database for Global Atmospheric Research version 5 (EDGARv5) (0.1°), EDGAR-downscaled (0.01°). For China and North and South Korea the surface emissions are taken from REAS (Regional Emission Inventory in Asia) with 0.25° × 0.25° resolution (Kurokawa and Ohara, 2020). The surface emission over Russia are taken from EDGARv5.

The EAGrid is the anthropogenic emission inventory for Japan (Kannari et al., 2007; Fukui et al., 2014) with a 1 km × 1 km resolution and monthly, hourly, and weekday/holiday variations for the base year 2010. The EDGARv5 inventory provides emissions for individual sectors at the spatial resolution of 0.1° × 0.1° on an annual basis for 1970 - 2015 and on a monthly basis for 2010 only. We use EDGARv5 and EDGAR-downscaled emission for the year 2015 in this work. The EDGAR-downscaled inventory (1 km grid or equivalent 0.01 degree) is created by redistributing the different sectors in the EDGAR emission inventory such as: (1) redistributing the energy and industry sectors by additional information of power plants (the location of power plants (coal, gas, oil) are taken from "A Global Database of Power Plants" (https://datasets.wri.org/dataset/) and Wikipedia "Lists of power stations") and of locations of facilities (https://mrdata.usgs.gov/mineral-operations/), (2) redistributing the transport sector by weighting the length of the road network and the information of each road (ranks of highways, national roads, urban roads, etc.) (the road networks are taken from "OpenStreetMap (OSM)"), (3) redistributing the RCO (residential and commercial buildings) using population distribution, and (4) redistributing the agricultural sector by the area of farmland. The distributions of the crops, grassland, and paddy are taken from "Land Cover (GLCNMO) – Global version, Version3". The location of the monthly burned areas is taken from "MODIS MCD64A1v006". The downscaled emission fraction exceeded 80% of the original total amount.

We applied the diurnal variation in CO_2 for EDGARv5 and EDGAR-downscaled emissions inventories based on the weights used for the treatment of hourly CO emissions to EAGrid2000 (Kannari et al., 2007). We have displayed the diurnal cycle for different anthropogenic emission

inventories used in WRF-GHG simulation for May 2018 in the supporting information Figure S1 for three CO_2 concentration observation sites (mentioned in Section 2.3).

The Fire INventory from NCAR (FINN; Wiedinmyer et al., 2011) biomass burning emissions ($0.1^o \times 0.1^o$) are used as input to WRF-GHG. CO_2 emission data for ocean is taken from Surface Ocean CO_2 Atlas (SOCAT) (Fay et al., 2021; spatial resolution: $1^o \times 1^o$). We have shown the CO_2 ocean flux projected over different domains in supporting information Figure S2**.**

2.3 CO_2 concentration observation data

Atmospheric CO_2 hourly concentration in-situ data is analyzed at Mt. Dodaira (36.00°N, 139.19°E, altitude; 852 m), Kisai (36.10°N, 139.57°E, altitude; 34 m), and Yoyogi (35.66°N, 139.68°E, altitude; 39 m). The in-situ CO_2 concentration data recorded with VIA-510R (HORIBA Ltd.) with measurement uncertainty of ~0.3 ppm at Mt. Dodaira and Kisai observations sites is obtained from the World Data Centre for Greenhouse Gases (WDCGG) operated by the Japan Meteorological Agency (JMA). On the other hand, the CO_2 concentration data at Yoyogi observation site is obtained from National Institute for Environmental Studies (NIES), Japan (Sugawara et al., 2021), using LI-820 (LI-COR) with reproducibility of 0.06 ppm for two-min averaged values. We also use CONTRAIL Continuous CO_2 Measuring Equipment (CME) CO_2 concentration data aboard Japan Airlines' commercial airliner flights (Machida et al., 2008). We also used Orbiting Carbon Oservatory-2 (OCO-2) satellite XCO_2 concentration (Eldering et al., 2017) observations (version 10) to evaluate WRF-GHG performance. OCO-2 was launched in launched in July 2014, OCO-2 is an Earth observing satellite mission owned and operated by NASA (National Aeronautics and Space Administration). OCO-2 spatial resolution is 1.29 km cross-track and 2.25 km along-track.

3. Results and Discussion

We performed high-resolution modeling to improve the representation of topographic complexity, synoptic weather conditions, and mesoscale transport of CO_2 and the CO_2 exchange flux between the biosphere and atmosphere. Figure 1a depicts WRF-GHG domain configurations and terrain height, while in Figure 1b, we zoomed into the inner-most domain and illustrated various land-use categories and in-situ measurement sites. To evaluate the model CO_2 concentration, we used surface observation sites Kisai (KIS), Mt. Dodaira (DDR), and Yoyogi (YYG) as shown in Figure 1b. We also evaluated the NEE calculated from the model using CO_2 flux observation sites Fuji Hokuroku (FHK: 35.44°N, 138.76°E, altitude; 1100 m) and Mase paddy (MSE: 36.03°N, 140.01°E, altitude; 11 m). Additionally, Figure 1b displays the CONTRAIL CO_2 concentration observations tracks for flights arriving and departing from the Haneda (HND) airport in Japan, with the blue color indicating flight altitude.

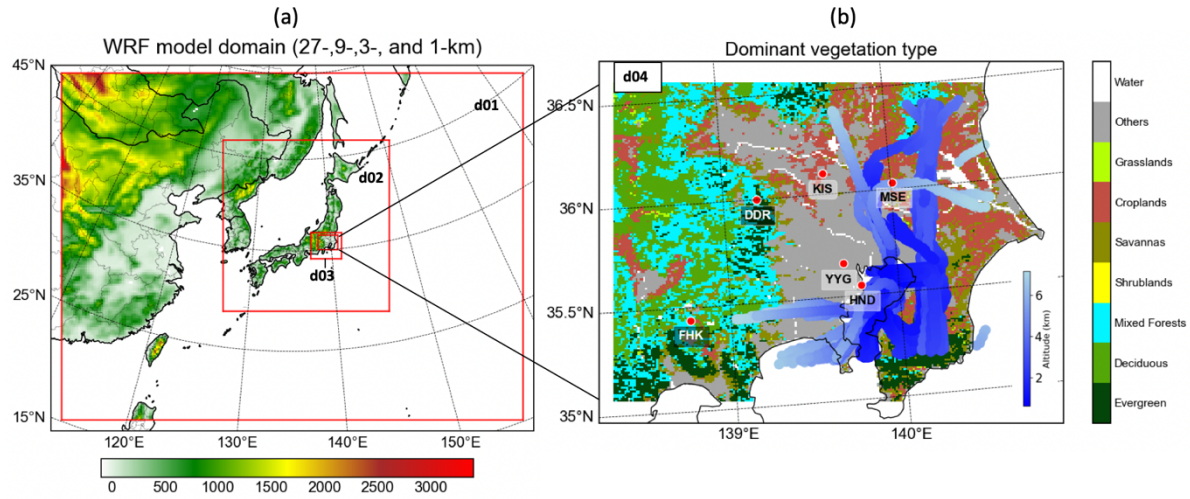

Figure 1: (a) The diagram illustrates the domain configurations for the model simulations (four domains: 27, 9, 3, and 1 km) and displays the terrain height for each domain. (b) The innermost domain in the diagram displays the dominant vegetation type used for VPRM calculation (derived from MODIS data) and observation sites for surface CO_2 concentration: Kisai (KIS), Mt. Dodaira (DDR), and Yoyogi (YYG). Additionally, the diagram shows CO_2 surface flux sites such as Fuji Hokuroku (FHK) and Mase paddy (MSE). The diagram also includes CONTRAIL CO_2 concentration observations for flights arriving and departing from Haneda (HND) airport in Japan. The blue color on the diagram represents the flight altitude.

The model NEE calculation has been evaluated against the available CO_2 flux tower data within the innermost domain (Fig. 1b). We have included a comparison of the NEE calculated from WRF-GHG with the CO_2 flux observations from Fuji Hokuroku Deciduous needleleaf forest and Mase paddy ('FHK' and 'MSE'; see Fig. 1b) in the supporting information (Fig. S3). VPRM parameter 'PAR_0' (Eq. 2) for the "deciduous forest" is taken from Li et al., 2020, and VPRM parameters 'λ' and 'α' for 'cropland type' (rice paddy) are taken '-0.1209' and '0.2100' respectively, based on iterative calculation to better fit WRF-GHG NEE to observed 'mase paddy' flux data (supporting information; Fig. S3). Other VPRM parameters are kept as 'default'. Note that in case of rice paddy, VPRM parameters for 'cropland type' may need to further tuned based on the rice growing season that takes place from May through September for most prefectures in Japan.

Figure 2 presents spatial maps of diurnal variations of CO_2 concentration and fluxes on May 9, 2018 (date chosen randomly), within the innermost domain. During May the land biosphere is more active compare to February (Supporting Information Fig. S4a and b). The leftmost four panels (Fig. 2a) display the diurnal variation in CO_2 concentrations at the surface layer, as modeled by WRF-GHG. The diurnal variation in surface CO_2 concentrations is influenced by PBL height and CO_2 emission

from ecosystem respiration process (Fig. 2c), resulting in higher atmospheric CO_2 concentrations at 00 and 06 JST (Japan Standard Time).

Figure 2b presents the diurnal variation in anthropogenic emissions (EAGrid) at the surface level, which peak at 12 and 18 JST. Figure 2c presents the diurnal variation of natural CO_2 fluxes over land and ocean. We did not detect a discernible CO_2 flux over the ocean within the innermost domain, as shown in supporting information Figure S2. At 12 and 18 JST, we noticed a predominance of CO_2 uptake attributable to photosynthesis activity, while CO_2 emission due to the ecosystem respiration process dominated at 00 and 06 JST, as shown in Figure 2c. Lastly, Figure 2d demonstrates the total CO_2 fluxes, which comprise mainly anthropogenic and natural land fluxes (ocean fluxes are masked out for domain 04 due to coarser resolution ($1^o \times 1^o$); supporting information Fig. S2).

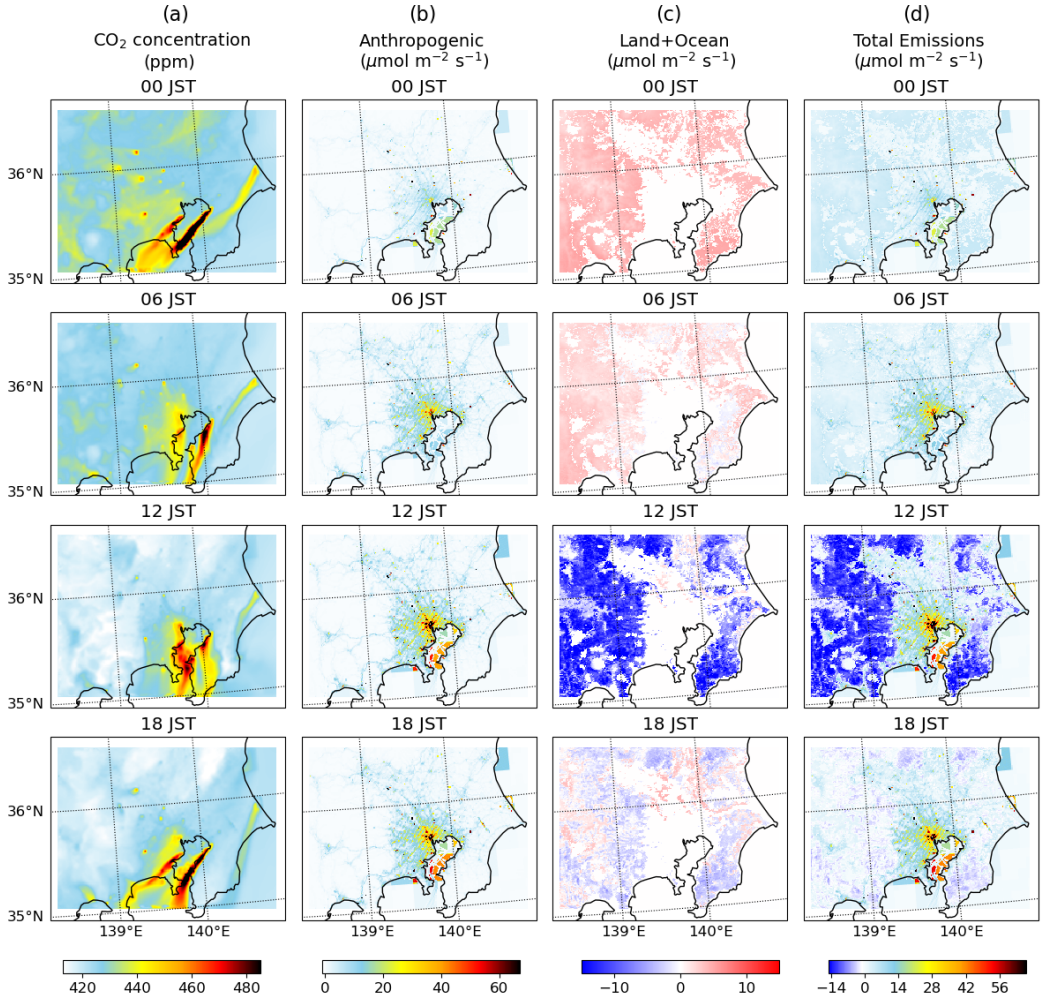

Figure 2: Six hourly spatial distribution maps on May 9, 2018 for inner most domain (1 km), depicting (a) atmospheric CO_2 concentration, (b) anthropogenic CO_2 emissions (EAGrid), (c) CO_2 emissions from land and ocean sources, and (d) total CO_2 emissions.

3.1 Model results evaluation with surface-based CO_2 concentration observations

We compared the WRF-GHG simulation results for inner most domain (1 km; Fig. 1b) with hourly in-situ observations at Kisai and Mt. Dodaira, and Yoyogi during February and May 2018 (Fig. 3 and 4). The Yoyogi station data is available during growing season (April-May) only. The total anthropogenic CO_2 emission for the inner-most domain (d04: Fig. 1b) is estimated to be 274.10, 332.20, 340.00 Tg (Tera-gram carbon unit) for EAGrid, EDGAR, and EDGAR-downscaled anthropogenic emission inventory, respectively.

The WRF-GHG model's results have been evaluated using basic statistical measures, such as root mean square error (RMSE; $\left[\sum_{i=1}^{N}\frac{(M_i-O_i)^2}{N}\right]^{1/2}$), and the mean bias ($\frac{\sum_{i=1}^{N}(M_i-O_i)}{N}$), where, M_i and O_i indicate hourly modeling results and observations, respectively. We have also evaluated the model performance using correlation coefficient (r; $\frac{\sum_{i=1}^{N}(M_i-\bar{M})(O_i-\bar{O})}{\sqrt{\sum_{i=1}^{N}(M_i-\bar{M})^2}\sqrt{\sum_{i=1}^{N}(O_i-\bar{O})^2}}$) between model and observations. Where $\bar{M}$ and $\bar{O}$ are the average of model simulations and observations, respectively.

In February 2018 (Fig. 3), there were no significant differences among model simulations from various anthropogenic emission inventories. However, in terms of correlation coefficient between model simulations and observations EAGrid and EDGAR performs better than EDGAR-downscaled anthropogenic emission inventory for Kisai and Mt. Dodaira. The model simulations (with all the anthropogenic emission inventories) showed underestimation for Kisai (Fig. 3a) and a minor overestimation for Mt. Dodaira (Fig. 3b).

During May 2018 (Fig. 4), the model simulations with EAGrid and EDGAR anthropogenic emission inventories exhibited a minor underestimation at Kisai (Fig. 4a). The RMSE in model simulations with all anthropogenic emission inventories at all in-situ observation sites is larger than that in February 2018 due to the presence of more active land-biosphere fluxes. Additionally, in Dodaira and Yoyogi observation sites (Figs. 4b and 4c), the model showed overestimation with all anthropogenic emission inventories, and the correlation between model simulations and observations is weak. However, the correlation between model simulations and observations is comparable between EAGrid and EDGAR (model simulations with EDGAR-downscaled exhibits weaker correlation) at Kisai (Fig. 4a). At Yoyogi correlation is better with the EAGrid (Fig. 4c) compared to EDGAR and EDGAR-downscaled anthropogenic emission inventories.

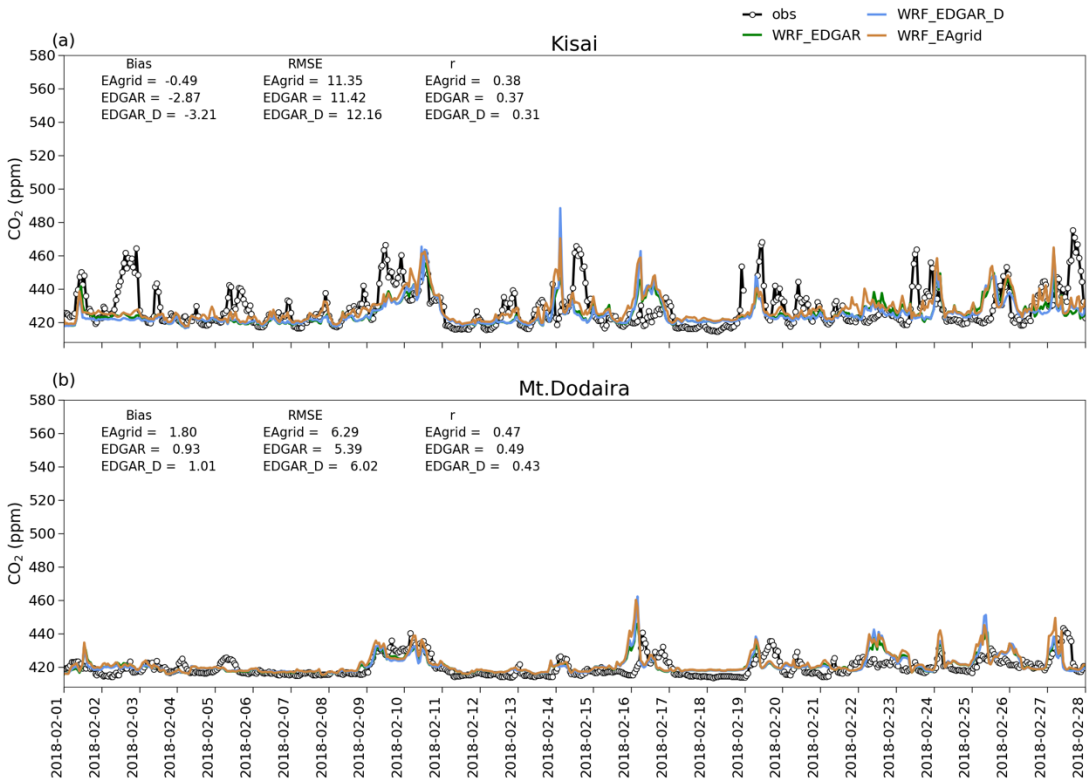

257

258 **Figure 3:** Hourly CO_2 concentrations at Kisai and Mt. Dodaira observation sites during February
259 2018. The observations (black) shown along with model simulation with EAGrid (orange), EDGAR
260 (green), EDGAR-Downscaled (EDGAR-D; blue) anthropogenic emission inventories. Statistics of
261 model observation comparison is given within each panel for different anthropogenic emission

inventories.

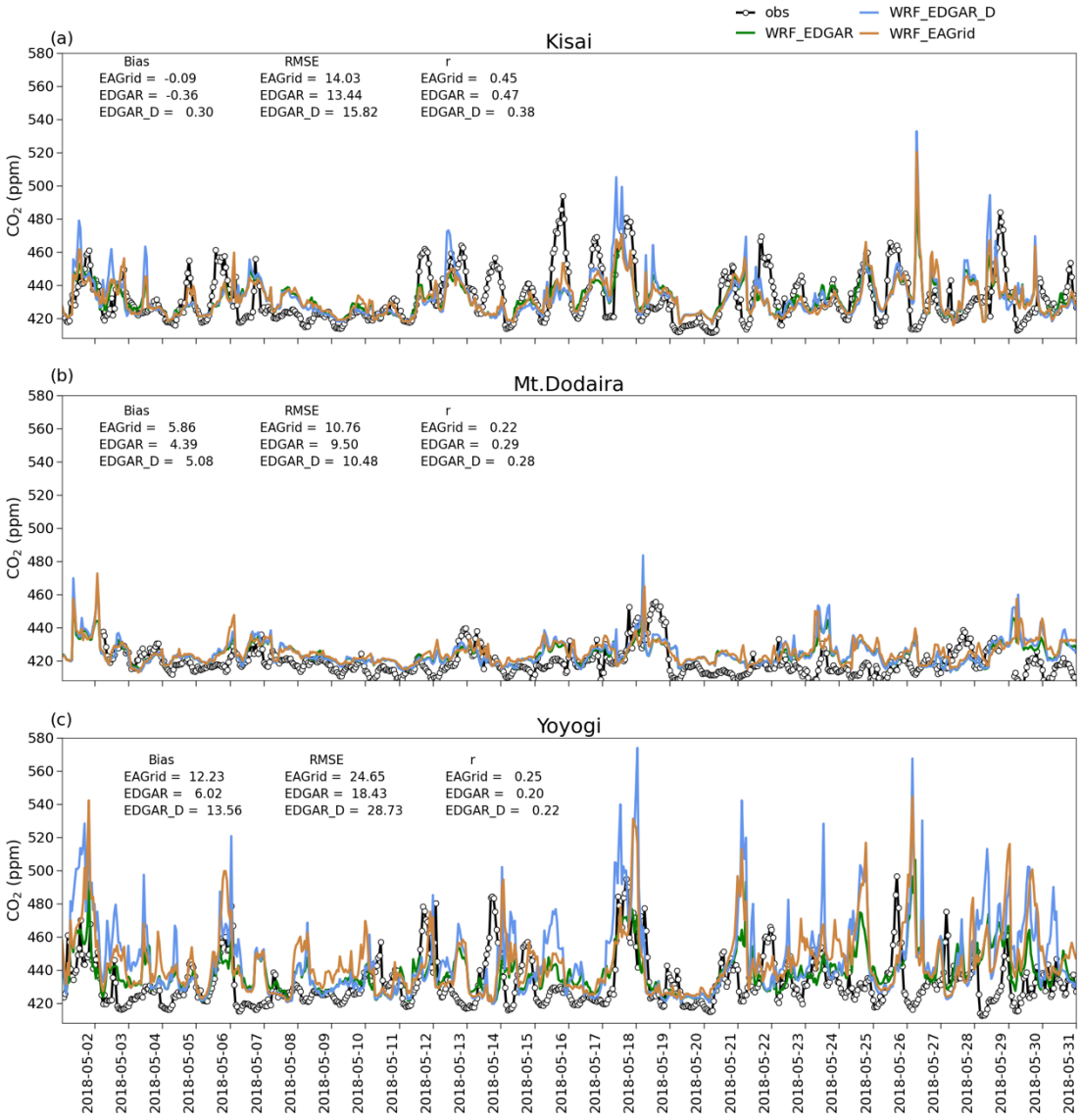

Figure 4: Same as Figure 3 but for May 2018 and Yoyogi observation site added.

Figure 5 presents the diurnal cycle of CO_2 during February and May 2018 over the mentioned in-situ observation sites. In February 2018 at Mt. Dodaira observation site, WRF-GHG (with all anthropogenic emission inventories) reasonably reproduced the observed diurnal variability ($r \geq 0.58$). However, at the Kisai observation site, WRF-GHG underestimated the CO_2 concentration during the night and overestimated it during the day. In Figure S4a of the supporting information, we demonstrated that anthropogenic emissions were the primary contributors to CO_2 emissions during February 2018. One potential explanation for the observed discrepancy between observed and modeled CO_2 concentrations at Kisai observation site is transport errors. For example, as shown in Figure 3 on February 2-3 and February 14-15, 2018, the model did not capture the strong CO_2 concentration peaks, which are possibly caused by transport errors. Another possibility is that

anthropogenic emission inventories do not adequately account for local or nearby CO_2 emissions, leading to underestimation of CO_2 concentrations.

During May 2018, at the Kisai site, the WRF-GHG model reproduced the diurnal variation ($r \geq 0.63$) but noticeably underestimated the peak-to-trough CO_2 amplitude during the night and day, likely due to a less intense NEE by VPRM from the model. Smaller PBL height change during day and night could also cause the underestimation in diurnal cycle for a given VPRM flux. The WRF-GHG simulations with EAGrid anthropogenic emission inventory better capture the diurnal variation at Kisai ($r = 0.95$) compared to EDGAR ($r = 0.85$) and EDGAR-downscaled ($r = 0.63$) anthropogenic emission inventories.

Over Mt. Dodaira, all model simulations overestimated CO_2 concentrations at all hours. However, simulations that used EDGAR ($r = 0.65$) and EDGAR-downscaled ($r = 0.66$) emission inventories performed better than those using EAGrid ($r = 0.11$). Similarly, over Yoyogi, the model simulations using EAGrid and EDGAR-downscaled emission inventories overestimated CO_2 concentrations. However, the CO_2 diurnal variation phase better matched with the model simulation using EAGrid anthropogenic emission inventory, resulting in a higher correlation ($r = 0.80$) with the observations. Model simulation with EDGAR anthropogenic emission inventory is closer to the observation during 00 to 08 JST but overestimated the CO_2 concentration during the rest of the hours.

We have shown the contribution of different tracers to total CO_2 concentration variability during May 2018 for Kisai, Mt. Dodaira, and Yoyogi in supporting information (Table S1). We found that major contribution to all the sites is from anthropogenic CO_2 tracer. Over Mt. Dodaira there is slightly negative contribution from land biosphere but it is very small in comparison to anthropogenic tracer. Therefore, the transport of anthropogenic emissions by local circulation (for e.g., land-sea-breeze) is a key factor in deciding the diurnal cycle in CO_2 concentration over these sites.

Overall, our analysis of CO_2 diurnal cycle exhibits prominent diurnal changes, with larger variations in May compared to February. During the daytime, specifically in May, lower CO_2 concentrations in the observations can be attributed to photosynthetic uptake and the PBL height, which allows for rapid vertical mixing between the near-surface and upper air. At night, larger CO_2 concentrations result from ecosystem respiration and a shallow PBL. The impact of PBL height on the diurnal variation of atmospheric CO_2 has been analyzed in multiple prior studies (for e.g., Dong et al., 2021; Hu et al., 2020; Ballav et al., 2016). We also discussed this phenomenon while explaining the spatial distribution of CO_2 concentration diurnal variation in Figure 2 in Section 3. Ballav et al. (2016) emphasized that number of layers in the WRF model needs to be increased, particularly below 200 m, to better resolve the PBL.

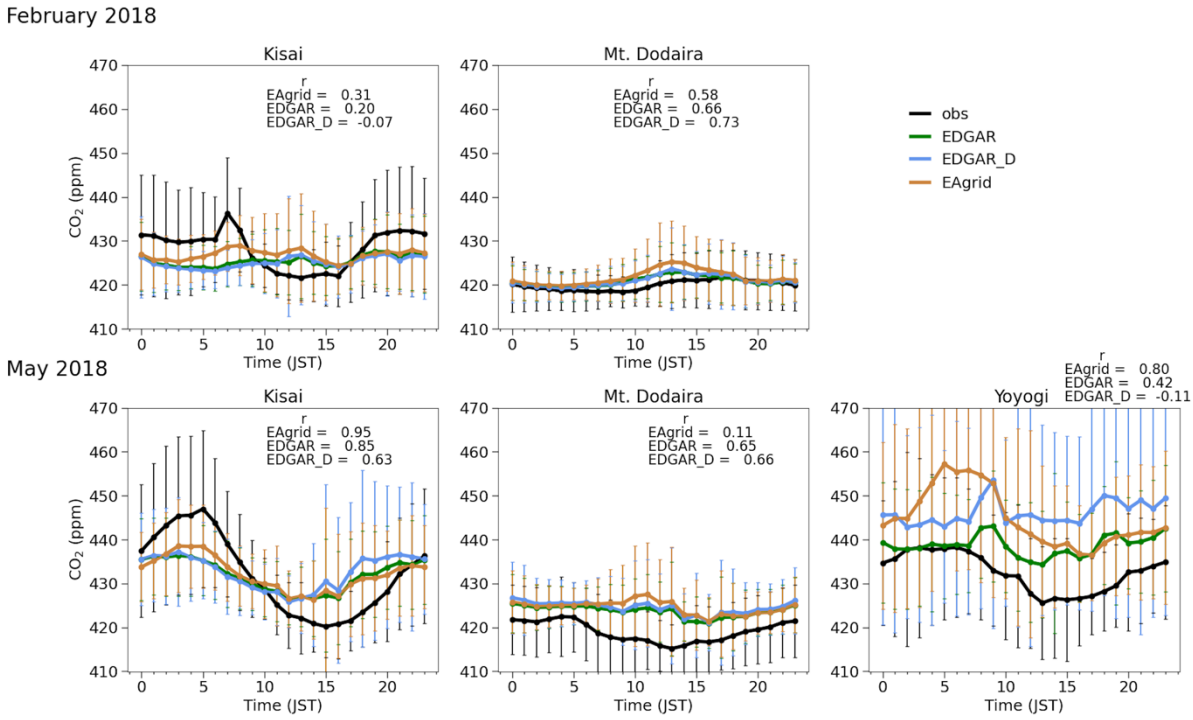

Figure 5: The comparison in the diurnal variation of CO_2 levels as observed and simulated using different anthropogenic emission inventories for February and May 2018. The error bars represent the standard deviation, and each panel includes the r (correlation coefficient) for the model simulations with different anthropogenic emission inventories.

3.2 Comparison between coarser and high-resolution CO_2 simulations with surface observations

We compared the WRF-GHG simulation for two spatial resolutions; coarser resolution (27 km) and finer resolution (1 km). In the case of coarser resolution, the model simulations are performed for the outermost domain independently (Fig. 1a; 27 km) during February 2018 without taking other domains into account. The finer domain simulation (1 km) results used here are the same as shown in Figure 3.

It could be noted from Figures 6a and 6b that, in the case of 1 km high-resolution model simulations, the model simulated CO_2 spread is larger compared to the 27 km model simulations which results in a better correlation coefficient in the case of 27 km model simulation specifically over Kisai (Fig. 6a). However, the slope is significantly underestimated in the case of 27 km model simulation compared to 1 km model simulations suggesting the significant underestimation of the observed variabilities (also shown in supporting information Fig. S5a). The slopes are calculated using the Orthogonal Distance Regression method (ODR) (Zhang et al., 2019) to better account for the variabilities present both in observations and model simulations. We may notice the instances (supporting information

Fig. S5a; February 15-17, 2018) where 1 km model simulations significantly overestimated the observed CO_2 concentration.

In the case of Mt Dodaira (Fig. 6b), the correlation between observed and simulated CO_2 concentration is comparable for 27 km and 1 km model simulations. However, in the case of 1 km model simulations, the slope is significantly improved compared to 27 km model simulations. We could also notice from supporting information Figure S5b, the large CO_2 peak between February 09, 2018, to February 11, 2018, is highly underestimated in the case of the 27 km model simulation, but better captured by the 1 km model simulation. For some days (for e.g., supporting information Figure S5b; Feb 15-17, 2018, Feb 22-23, 2018), CO_2 concentration was significantly overestimated in the case of high-resolution (1 km) simulation.

The analysis suggests that high-resolution model simulations (1 km) at Kisai observation site are more scattered compared to Mt. Dodaira. One of the reasons is Kisai site is more influenced by the transport from high emission sources from the Tokyo area by the local atmospheric circulations compared to Mt. Dodaira which is located in a remote location with an altitude of 852 m. The analysis needs expansion for more spatial observation coverage to illustrate the full potential of high-resolution model simulations. It is also needed to examine in the following study whether the high-resolution simulation amplifies the systematic bias present in the forcing parameters used for nudging the model.

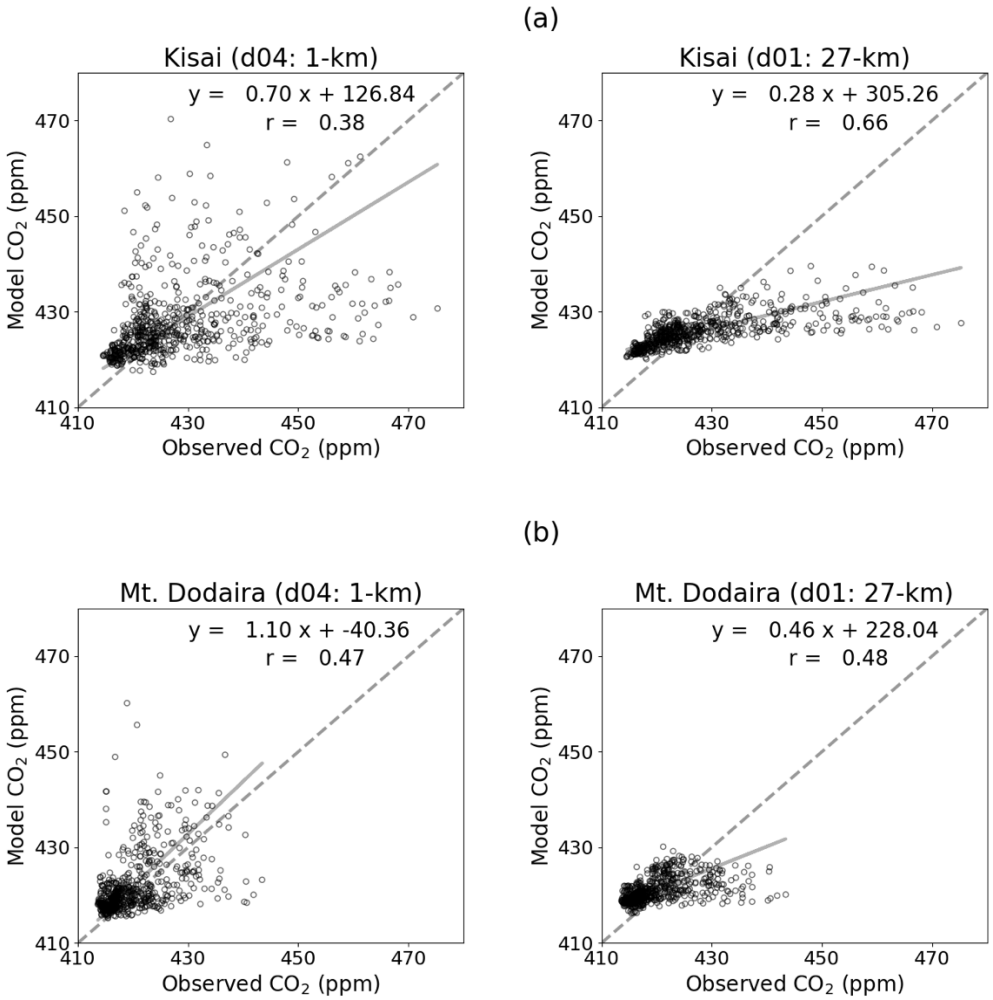

Figure 6: Scatter diagram between observed and simulated CO_2 during February 2018 for: (a) finer (1 km) and coarser (27 km) model domains over Kisai, (b) finer and coarser model domains over Mt. Dodaira. The dashed line is 1:1 line

3.3 Model results evaluation with aircraft observations of CO_2 concentrations

Figure 7a show the WRF-GHG simulations comparison with CONTRAIL aircraft observations during February 2018 (Number of data points (N) = 2368). We first spatio-temporally collocate the model and CONTRAIL CO_2 concentration observation and then binned CO_2 observations at each 100 m altitude starting from 700 m altitude (total 65 layers). It is worth noting that all emission inventories produce comparable results during February 2018 (Fig. 7a). To investigate the performance of the model's CO_2 concentration regarding the contribution of different tracers, we displayed the background and land biosphere (background + land biosphere) contribution separately for February 2018 (Fig. 7b). Figure 7b indicates that the primary contribution to CO_2 concentration variation during February 2018 could be attributed to anthropogenic tracer from the altitude range near the surface to 3200 m. The background and land biosphere CO_2 tracers merged throughout the vertical

profile during February 2018, which suggests no noticeable contribution from the land biosphere tracer. Furthermore, it is noteworthy that after a certain altitude (>3200 m), the CO_2 concentration from the background and land biosphere merged with the total CO_2 concentration. This signifies the impact of lateral boundaries, and WRF-GHG is able to reproduce the CO_2 variation well, including the plume-like signature near the top of the CO_2 profile (6600-7200 m altitude range; Figs. 7a and 7b).

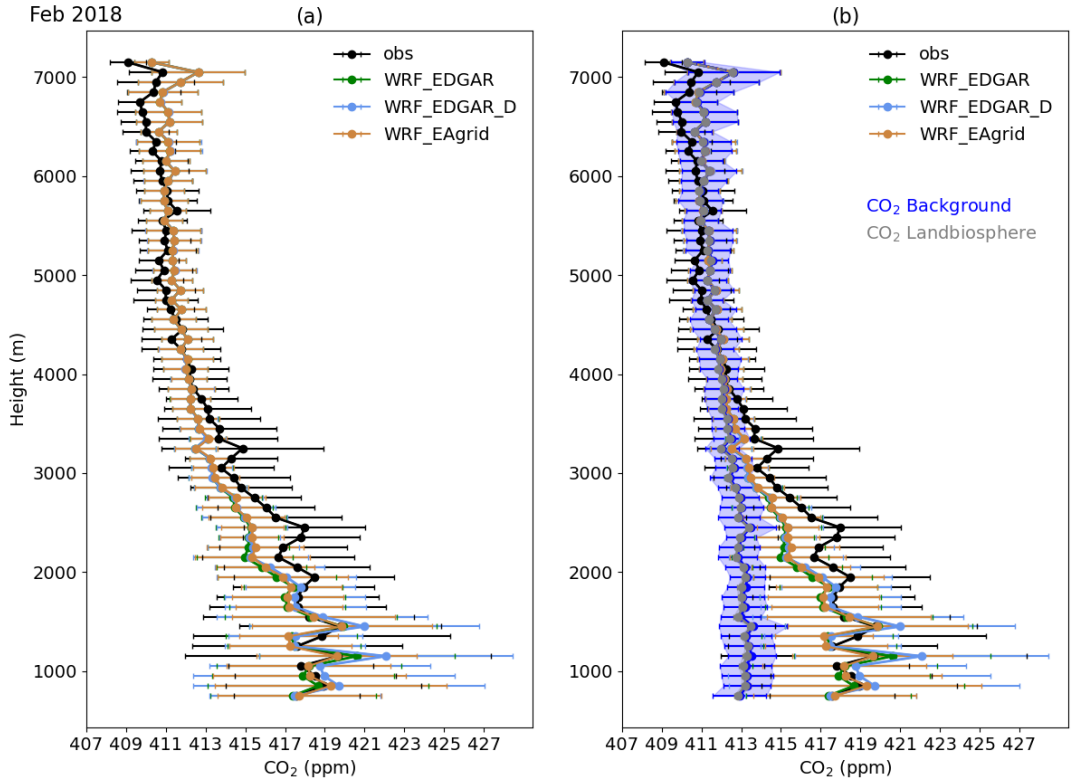

Figure 7: Comparison of CO_2 Vertical Distribution in February 2018: (a) CONTRAIL observations and sensitivity of simulations to anthropogenic emission inventories, (b) same as '(a)' but includes the contribution from background and land biosphere (background + land biosphere) tracers in vertical distribution of CO_2. The error bar represents the standard deviation.

We have also shown comparison of the vertical profile during May 2018 from both WRF-GHG and CONTRAIL observations in Figure 8a (N = 1778). Similar to February 2018, WRF-GHG reasonably reproduces the vertical distribution of CO_2, and no noticeable difference was found in model simulations with different anthropogenic emission inventories. Furthermore, our Figure 8b illustrates the model's CO_2 concentration regarding the contribution of different tracers during May 2018. Unlike February 2018, we may notice the dominant contribution of land biosphere tracer to the total CO_2 concentration during May 2018. Therefore, the total CO_2 concentration during May 2018 is a result of both anthropogenic and land biosphere flux, in addition to the background. The land biosphere tracer

to the total CO_2 concentration is up to an altitude of 4500 m and beyond that altitude, the main contributor was the background tracer.

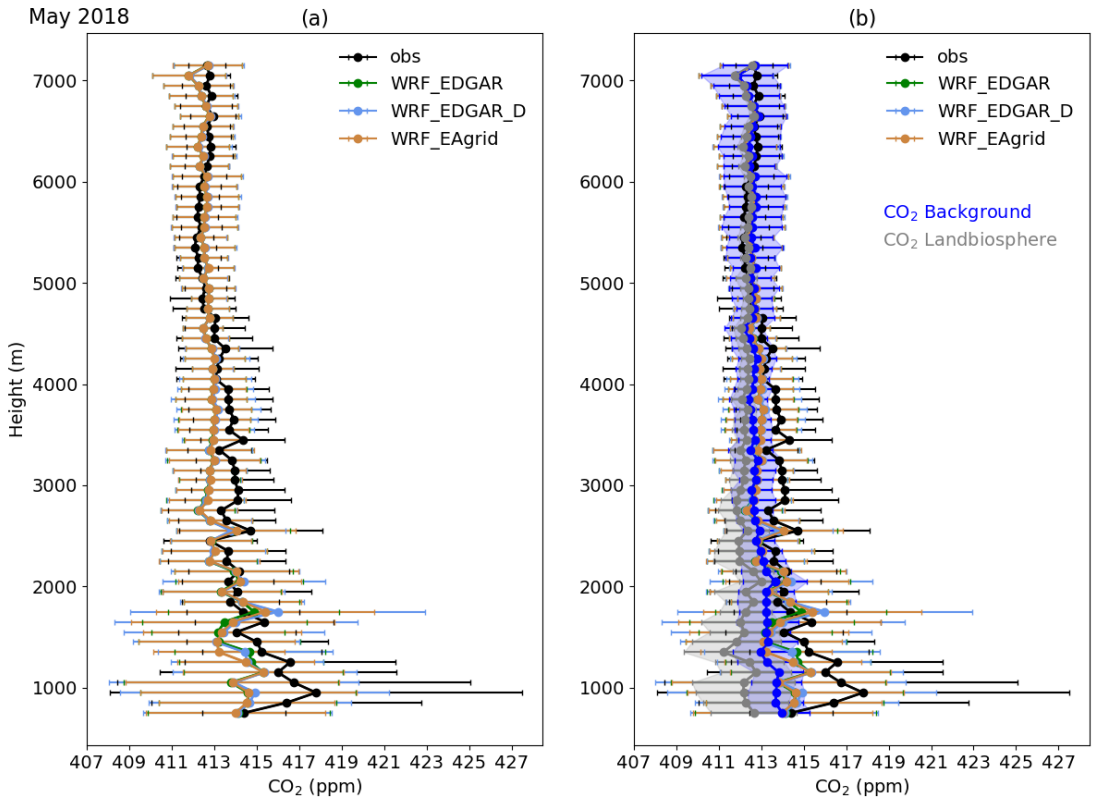

Figure 8: Same as Figure 7 but for May 2018.

We compared the WRF-GHG simulations with CONTRAIL aircraft observations for two spatial resolutions; coarser resolution (27 km) and finer resolution (1 km) (Fig. 9a). It may be noted that coarser resolution simulations largely underestimated the observed CO_2 concentration up to an altitude range of approximately 2400 m (Fig. 9a). Above that, the 1 km and 27 km model simulations are similar. The under-estimation of CO_2 concentration in coarser resolution WRF-GHG simulations could be attributed to the under-representation of fine scale vertical transport processes (Yamashita et al., 2021) such as: vertical diffusion and convection. On the other hand, 1 km simulations reasonably reproduced the observed variability in the vertical distribution of CO_2 concentration.

Our study also included a sensitivity analysis of boundary conditions, where we conducted CO_2 concentration simulations using fixed boundaries instead of MIROC4-ACTM (Fig. 9b). The analysis showed that, beyond an altitude of 3200 m, a systematic bias of approximately 4 ppm exists in the CO_2 profile when fixed (a constant value) boundary conditions are applied, as compared to the results obtained when using boundary conditions from MIROC4-ACTM. Furthermore, when using fixed lateral boundary conditions, plume-like signatures as observed in the CO_2 profile around 7000 m (Fig.

9b) are not reproduced. We conclude that the selection of a model field with a wider domain (MIROC4-ACTM for this study) for lateral boundary conditions to WRF-GHG is critically important. In a recent study conducted by Munassar et al., 2023, the influence of lateral boundary conditions on regional inversions was also highlighted, underscoring the importance of isolating the far-field contributions.

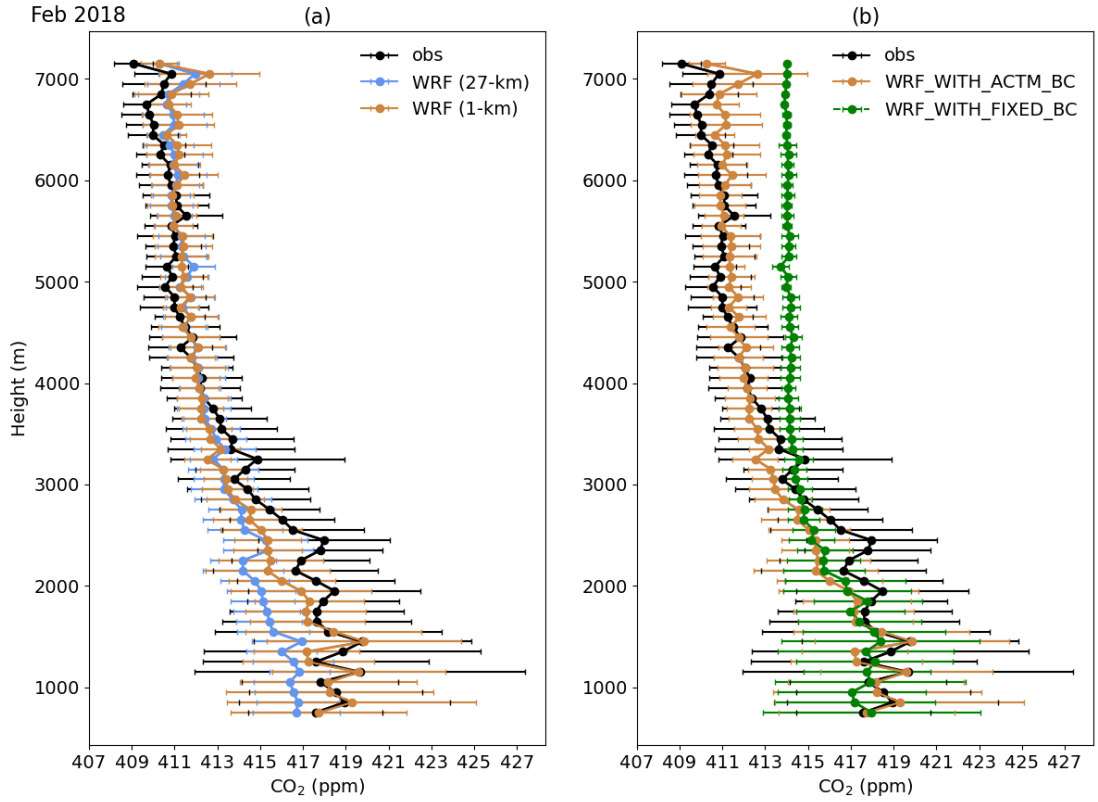

Figure 9: Comparison of CO_2 vertical distribution between CONTRAIL and WRF-GHG simulations during February 2018 for: (a) finer (1 km) and coarser (27 km) model domains, (b) fixed (a constant value) initial and lateral boundary conditions and with MIROC4-ACTM initial and lateral boundary conditions to WRF-GHG. The error bar represents the standard deviation.

3.4 Model results evaluation with satellite observations

The WRF-GHG model simulated column-averaged CO_2 concentrations (XCO_2) dataset that is spatiotemporally sampled with Orbiting Carbon Observatory-2 (OCO-2) observations as follows:

$$XCO_2 = XCO_{2(\text{a priori})} + \sum_j h_j \, a_j (CO_{2(\text{ACTM})} - CO_{2(\text{a priori})})_j$$

Where, XCO_2 is the column-averaged model simulated CO_2 concentration. XCO_2 (a priori) is a priori column-averaged concentration provided in the OCO-2 dataset. CO_2 (ACTM) and CO_2 (a priori) are

the CO_2 profile from ACTM and a priori (OCO-2 dataset), respectively. h_j is the pressure weighting function (j is the vertical layer index), and a_j represents averaging kernel matrix for the column retrieval which is the sensitivity of the retrieved total column at the various ('j') atmospheric levels (Bisht et al., 2023).

To compare with OCO-2 data, we used the CO_2 concentration simulations performed with EAGrid anthropogenic emission inventory within the second domain (9 km; Fig. 1a) due to limited spatial coverage of OCO-2. To calculate XCO_2 from WRF-GHG model output, we used CO_2 concentration data above 155 hPa (which is the top of the atmosphere in WRF-GHG) obtained from MIROC4-ACTM. Firstly, we performed spatio-temporal collocation of the model simulations and observations, and created a 0.25^o mesh for re-gridding the OCO-2 and model data (0.25 degrees re-gridding performed here since most of the data points fall under rural-remote regions; Figs. 10a and b). Next, we calculated the average data for the months of February and May 2018, as depicted in Figure 10. The white space in the figure represents no data.

During February 2018 (Fig. 10a), we found a correlation coefficient of 0.47 (N = 107) between the OCO-2 and model data, suggesting the reasonable performance by the model. However, in May 2018 (Fig. 10b), we found a weak correlation coefficient of 0.17 (N = 196) between OCO-2 and the model. One possibility of weak correlation during May is the more CO_2 sink produced by the VPRM than suggested by the observations over WRF-GHG simulation domains. We noticed a strong land biosphere sink in model simulations for the inner-most domain during May (Fig. 8b) while comparing the model simulation results with aircraft observations. The model underestimation of CO_2 concentration between 700 – 1500 m altitude range during May (Fig. 8b) could be attributed to more CO_2 sink produced by the model than suggested by the observations since during Feb (Fig. 7b) model simulations match well with the observations when land biosphere is less active. Also, the strong sink in the outermost domain (d01; Fig. 1a) could provide depleted CO_2 feedback to domain 2 in terms of boundary conditions that could further underestimate the CO_2 concentration.

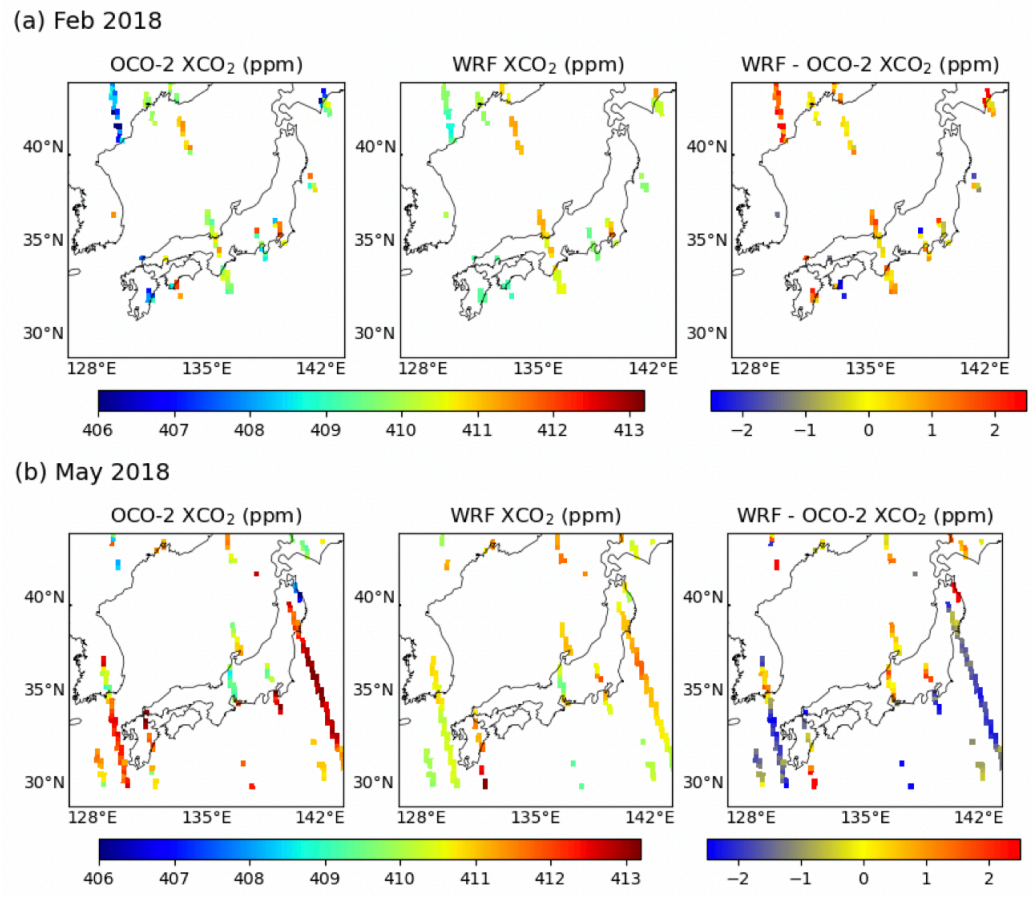

Figure 10: Comparison of the XCO_2 observed by the OCO-2 satellite and simulated by the WRF-GHG model: (a) Feb 2018 and (b) May 2018.

4. Summary

This study uses the WRF-GHG model to simulate atmospheric CO_2 using various anthropogenic emission inventories. The results obtained from the finest domain (1 km) were compared with in-situ surface and aircraft observations. The findings suggest that the WRF-GHG model, using different anthropogenic emission inventories, can reasonably replicate the observed variations in in-situ surface observation. Based on our sensitivity experiments and analysis for different in-situ surface sites for CO_2 concentration, we found EAGrid is a more appropriate anthropogenic emission inventory for Japan compared to the other two anthropogenic emission inventories used here.

We analyzed the difference in coarser (27 km) and finer (1 km) resolution model simulations based on surface observations and found a significant underestimation of CO_2 concentration in the case of 27 km model simulations compared to 1 km model simulations. Also, the observed variability in CO_2 concentration is better captured by high-resolution (1 km) model simulations. However, in some days during the simulation period, we noticed a significant CO_2 concentration overestimation in the case of

high-resolution (1 km) simulation. The full potential of high-resolution modeling needed to be evaluated with more spatial observation coverage in the following study.

The study evaluates the performance of the WRF-GHG model by comparing its output with CONTRAIL aircraft observations for February and May 2018. We compare the model simulations with different emission inventories to assess their consistency with the observations. The results show that all emission inventories produce comparable results during February and May 2018. Furthermore, the model reasonably reproduces the CO_2 variation, and the primary contribution (till 3200 m) to CO_2 concentration variation during February 2018 arises from the anthropogenic tracer. In May 2018, both anthropogenic and land biosphere tracers contributed to the total CO_2 concentration. The study also highlights the importance of lateral boundary conditions in modeling atmospheric CO_2 concentrations and shows that a systematic bias (~ 4 ppm) persists beyond an altitude of 3200 meters (February 2018) when fixed boundary conditions are applied.

We also analyzed the WRF-GHG simulations with CONTRAIL aircraft observations for coarser (27 km) and finer resolution (1 km) and demonstrates the advantage of 1 km simulation over 27 km simulations in reproducing the observed variability in the vertical distribution of CO_2 concentration. We found a large underestimation in CO_2 concentration in the coarser resolution (27 km) simulations below 2500 m altitude. We concluded that the under-representation of fine-scale transport processes (e.g., vertical diffusion, convection) of atmospheric CO_2 in the coarser resolution model simulation could underestimate the CO_2 concentration.

The study also compares XCO_2 from the OCO-2 satellite and the XCO_2 calculated from the WRF-GHG model output. The study found a reasonable performance of the model in February 2018 with a correlation coefficient of 0.47, but a weak correlation in May 2018 with a correlation coefficient of 0.17. Our results based on aircraft observations suggest dominant land biosphere activity during May which are not modeled well by WRF-GHG/VPRM. On the other hand, in the presence of less land biosphere activity during February model simulations match well with the observations.

Code and data availability. The WRF-Chem source code is archived at https://ruc.noaa.gov/wrf/wrf-chem/. Atmospheric CO_2 hourly concentration data for Mt. Dodaira and Kisai is archived at https://gaw.kishou.go.jp/ as Yosuke MUTO (SAIPF), Atmospheric CO_2 at Kisai by Center for Environmental Science in Saitama, dataset published as CO2_KIS_surface-insitu_SAIPF_data1 at WDCGG, ver. 2022-06-27-0532 (Reference date*: 2023/05/19) and Yosuke MUTO (SAIPF), Atmospheric CO2 at Mt. Dodaira by Center for Environmental Science in Saitama, dataset published as CO2_DDR_ surface-insitu_SAIPF_data1 at WDCGG, ver. 2022-06-27-0532 (Reference date*:

2023/05/19). Yoyogi station data is achieved at https://www.nies.go.jp/doi/10.17595/20210510.001-e.html. CONTRAIL Continuous CO_2 Measuring Equipment (CME) data aboard Japan Airlines' commercial airliner flights is archived at https://www.nies.go.jp/doi/10.17595/20180208.001-e.html. OCO2 satellite observation data is archived at https://ocov2.jpl.nasa.gov/. The eddy covariance datasets of MSE and FHK facilitated this study. The MSE data is obtained from AsiaFlux Database (http://asiaflux.net). The CO_2 flux data at FHK site is archived at: Takahashi (2021), Micrometeorological CO_2 Flux Data at Fuji Hokuroku Flux Observation Site (FHK), Ver.2.1, National Institute for Environmental Studies, DOI:10.17595/20210730.001, (Reference date*: 2023/05/19)

Acknowledgements. We thank to Saitama Prefecture and WDCGG for providing the CO_2 concentration data for Kisai and Mt. Dodaira. We thank to NIES, Japan for providing the CO_2 concentration data for Yoyogi. We are thankful to engineers and staffs of the Japan Airlines, JAL Foundation, and JAMCO Tokyo for supporting the CONTRAIL project. The authors acknowledge the efforts of NASA to provide the OCO-2 data products. This research has been supported by GOSAT-GW project.

References

Ahmadov, R., Gerbig, C., Kretschmer, R., Koerner, S., Neininger, B., Dolman, A. J., and Sarrat, C.: Mesoscale covariance of transport and CO 2 fluxes: Evidence from observations and simulations using the WRF-VPRM coupled atmosphere-biosphere model, J. Geophys. Res., 112, D22107, https://doi.org/10.1029/2007JD008552, 2007.

Ahmadov, R., Gerbig, C., Kretschmer, R., Körner, S., Rödenbeck, C., Bousquet, P., and Ramonet, M.: Comparing high resolution WRF-VPRM simulations and two global CO2 transport models with coastal tower measurements of CO2, Biogeosciences, 6, 807–817, https://doi.org/10.5194/bg-6-807-2009, 2009.

Ballav, S., Patra, P. K., Sawa, Y., Matsueda, H., Adachi, A., Onogi, S., Takigawa, M., and De, U. K.: Simulation of CO2 concentrations at Tsukuba tall tower using WRF-CO2 tracer transport model, J. Earth Syst. Sci., 125, 47–64, https://doi.org/10.1007/s12040-015-0653-y, 2016.

BALLAV, S., PATRA, P. K., TAKIGAWA, M., GHOSH, S., DE, U. K., MAKSYUTOV, S., MURAYAMA, S., MUKAI, H., and HASHIMOTO, S.: Simulation of CO2 Concentration over East Asia Using the Regional Transport Model WRF-CO2, J. Meteorol. Soc. Japan. Ser. II, 90, 959–976, https://doi.org/10.2151/jmsj.2012-607, 2012.

Bisht, J. S. H., Machida, T., Chandra, N., Tsuboi, K., Patra, P. K., Umezawa, T., Niwa, Y., Sawa, Y., Morimoto, S., Nakazawa, T., Saitoh, N., and Takigawa, M.: Seasonal Variations of SF 6 , CO 2 , CH

4 , and N 2 O in the UT/LS Region due to Emissions, Transport, and Chemistry, J. Geophys. Res. Atmos., 126, https://doi.org/10.1029/2020JD033541, 2021.

Bisht, J. S. H., Patra, P. K., Takigawa, M., Sekiya, T., Kanaya, Y., Saitoh, N., and Miyazaki, K.: Estimation of CH4 emission based on an advanced 4D-LETKF assimilation system, Geosci. Model Dev., 16, 1823–1838, https://doi.org/10.5194/gmd-16-1823-2023, 2023.

Dayalu, A., Munger, J. W., Wofsy, S. C., Wang, Y., Nehrkorn, T., Zhao, Y., McElroy, M. B., Nielsen, C. P., and Luus, K.: Assessing biotic contributions to CO2 fluxes in northern China using the Vegetation, Photosynthesis and Respiration Model (VPRM-CHINA) and observations from 2005 to 2009, Biogeosciences, 15, 6713–6729, https://doi.org/10.5194/bg-15-6713-2018, 2018.

Dong, X., Yue, M., Jiang, Y., Hu, X.-M., Ma, Q., Pu, J., and Zhou, G.: Analysis of CO2 spatio-temporal variations in China using a weather–biosphere online coupled model, Atmos. Chem. Phys., 21, 7217–7233, https://doi.org/10.5194/acp-21-7217-2021, 2021.

Duren, R. M. and Miller, C. E.: Measuring the carbon emissions of megacities, Nat. Clim. Chang., 2, 560–562, https://doi.org/10.1038/nclimate1629, 2012.

Eldering, A., O'Dell, C. W., Wennberg, P. O., Crisp, D., Gunson, M. R., Viatte, C., Avis, C., Braverman, A., Castano, R., Chang, A., Chapsky, L., Cheng, C., Connor, B., Dang, L., Doran, G., Fisher, B., Frankenberg, C., Fu, D., Granat, R., Hobbs, J., Lee, R. A. M., Mandrake, L., McDuffie, J., Miller, C. E., Myers, V., Natraj, V., O'Brien, D., Osterman, G. B., Oyafuso, F., Payne, V. H., Pollock, H. R., Polonsky, I., Roehl, C. M., Rosenberg, R., Schwandner, F., Smyth, M., Tang, V., Taylor, T. E., To, C., Wunch, D., and Yoshimizu, J.: The Orbiting Carbon Observatory-2: first 18 months of science data products, Atmos. Meas. Tech., 10, 549–563, https://doi.org/10.5194/amt-10-549-2017, 2017.

Fay, A. R., Gregor, L., Landschützer, P., McKinley, G. A., Gruber, N., Gehlen, M., Iida, Y., Laruelle, G. G., Rödenbeck, C., Roobaert, A., and Zeng, J.: SeaFlux: harmonization of air-sea CO2 fluxes from surface pCO2 data products using a standardized approach, Earth Syst. Sci. Data, 13, 4693–4710, https://doi.org/10.5194/essd-13-4693-2021, 2021.

Friedlingstein, P., O'Sullivan, M., Jones, M. W., Andrew, R. M., Gregor, L., Hauck, J., Le Quéré, C., Luijkx, I. T., Olsen, A., Peters, G. P., Peters, W., Pongratz, J., Schwingshackl, C., Sitch, S., Canadell, J. G., Ciais, P., Jackson, R. B., Alin, S. R., Alkama, R., Arneth, A., Arora, V. K., Bates, N. R., Becker, M., Bellouin, N., Bittig, H. C., Bopp, L., Chevallier, F., Chini, L. P., Cronin, M., Evans, W., Falk, S., Feely, R. A., Gasser, T., Gehlen, M., Gkritzalis, T., Gloege, L., Grassi, G., Gruber, N., Gürses, Ö., Harris, I., Hefner, M., Houghton, R. A., Hurtt, G. C., Iida, Y., Ilyina, T., Jain, A. K., Jersild, A., Kadono, K., Kato, E., Kennedy, D., Klein Goldewijk, K., Knauer, J., Korsbakken, J. I., Landschützer, P., Lefèvre, N., Lindsay, K., Liu, J., Liu, Z., Marland, G., Mayot, N., McGrath, M. J., Metzl, N., Monacci, N. M., Munro, D. R., Nakaoka, S.-I., Niwa, Y., O'Brien, K., Ono, T., Palmer, P. I., Pan, N., Pierrot, D., Pocock, K., Poulter, B., Resplandy, L., Robertson, E., Rödenbeck, C.,

Rodriguez, C., Rosan, T. M., Schwinger, J., Séférian, R., Shutler, J. D., Skjelvan, I., Steinhoff, T., Sun, Q., Sutton, A. J., Sweeney, C., Takao, S., Tanhua, T., Tans, P. P., Tian, X., Tian, H., Tilbrook, B., Tsujino, H., Tubiello, F., van der Werf, G. R., Walker, A. P., Wanninkhof, R., Whitehead, C., Willstrand Wranne, A., et al.: Global Carbon Budget 2022, Earth Syst. Sci. Data, 14, 4811–4900, https://doi.org/10.5194/essd-14-4811-2022, 2022.

Fukui, T., Kokuryo, K., Baba, T., and Kannari, A.: Updating EAGrid2000-Japan emissions inventory based on the recent emission trends, J. Japan Soc. Atmos. Environ., 49, 117–125, https://doi.org/10.11298/taiki.49.117, 2014.

Grell, G. A. and Dévényi, D.: A generalized approach to parameterizing convection combining ensemble and data assimilation techniques, Geophys. Res. Lett., 29, 38-1-38–4, https://doi.org/10.1029/2002GL015311, 2002.

Gurney, K. R., Liang, J., Patarasuk, R., Song, Y., Huang, J., and Roest, G.: The Vulcan Version 3.0 High-Resolution Fossil Fuel CO 2 Emissions for the United States, J. Geophys. Res. Atmos., 125, https://doi.org/10.1029/2020JD032974, 2020.

Hu, X., Crowell, S., Wang, Q., Zhang, Y., Davis, K. J., Xue, M., Xiao, X., Moore, B., Wu, X., Choi, Y., and DiGangi, J. P.: Dynamical Downscaling of CO 2 in 2016 Over the Contiguous United States Using WRF-VPRM, a Weather-Biosphere-Online-Coupled Model, J. Adv. Model. Earth Syst., 12, https://doi.org/10.1029/2019MS001875, 2020.

Huo, D., Huang, X., Dou, X., Ciais, P., Li, Y., Deng, Z., Wang, Y., Cui, D., Benkhelifa, F., Sun, T., Zhu, B., Roest, G., Gurney, K. R., Ke, P., Guo, R., Lu, C., Lin, X., Lovell, A., Appleby, K., DeCola, P. L., Davis, S. J., and Liu, Z.: Carbon Monitor Cities near-real-time daily estimates of CO2 emissions from 1500 cities worldwide, Sci. Data, 9, 533, https://doi.org/10.1038/s41597-022-01657-z, 2022.

Janssens-Maenhout, G., Crippa, M., Guizzardi, D., Muntean, M., Schaaf, E., Dentener, F., Bergamaschi, P., Pagliari, V., Olivier, J. G. J., Peters, J. A. H. W., van Aardenne, J. A., Monni, S., Doering, U., Petrescu, A. M. R., Solazzo, E., and Oreggioni, G. D.: EDGAR v4.3.2 Global Atlas of the three major greenhouse gas emissions for the period 1970–2012, Earth Syst. Sci. Data, 11, 959–1002, https://doi.org/10.5194/essd-11-959-2019, 2019.

Kannari, A., Tonooka, Y., Baba, T., and Murano, K.: Development of multiple-species 1km×1km resolution hourly basis emissions inventory for Japan, Atmos. Environ., 41, 3428–3439, https://doi.org/10.1016/j.atmosenv.2006.12.015, 2007.

Kurokawa, J. and Ohara, T.: Long-term historical trends in air pollutant emissions in Asia: Regional Emission inventory in ASia (REAS) version 3, Atmos. Chem. Phys., 20, 12761–12793, https://doi.org/10.5194/acp-20-12761-2020, 2020.

589 Lauvaux, T., Miles, N. L., Deng, A., Richardson, S. J., Cambaliza, M. O., Davis, K. J., Gaudet, B.,
590 Gurney, K. R., Huang, J., O'Keefe, D., Song, Y., Karion, A., Oda, T., Patarasuk, R., Razlivanov, I.,
591 Sarmiento, D., Shepson, P., Sweeney, C., Turnbull, J., and Wu, K.: High-resolution atmospheric
592 inversion of urban CO2 emissions during the dormant season of the Indianapolis Flux Experiment
593 (INFLUX), J. Geophys. Res. Atmos., 121, 5213–5236, https://doi.org/10.1002/2015JD024473, 2016.

594 Li, X., Hu, X., Cai, C., Jia, Q., Zhang, Y., Liu, J., Xue, M., Xu, J., Wen, R., and Crowell, S. M. R.:
595 Terrestrial CO2 Fluxes, Concentrations, Sources and Budget in Northeast China: Observational and
596 Modeling Studies, J. Geophys. Res. Atmos., 125, https://doi.org/10.1029/2019JD031686, 2020.

597 Liu, Z., Guan, D., Wei, W., Davis, S. J., Ciais, P., Bai, J., Peng, S., Zhang, Q., Hubacek, K., Marland,
598 G., Andres, R. J., Crawford-Brown, D., Lin, J., Zhao, H., Hong, C., Boden, T. A., Feng, K., Peters, G.
599 P., Xi, F., Liu, J., Li, Y., Zhao, Y., Zeng, N., and He, K.: Reduced carbon emission estimates from
600 fossil fuel combustion and cement production in China, Nature, 524, 335–338,
601 https://doi.org/10.1038/nature14677, 2015.

602 Machida, T., Matsueda, H., Sawa, Y., Nakagawa, Y., Hirotani, K., Kondo, N., Goto, K., Nakazawa,
603 T., Ishikawa, K., and Ogawa, T.: Worldwide measurements of atmospheric CO 2 and other trace gas
604 species using commercial airlines, J. Atmos. Ocean. Technol., 25, 1744–1754,
605 https://doi.org/10.1175/2008JTECHA1082.1, 2008.

606 Mahadevan, P., Wofsy, S. C., Matross, D. M., Xiao, X., Dunn, A. L., Lin, J. C., Gerbig, C., Munger,
607 J. W., Chow, V. Y., and Gottlieb, E. W.: A satellite-based biosphere parameterization for net
608 ecosystem CO 2 exchange: Vegetation Photosynthesis and Respiration Model (VPRM), Global
609 Biogeochem. Cycles, 22, https://doi.org/10.1029/2006GB002735, 2008.

610 Morrison, H., Thompson, G., and Tatarskii, V.: Impact of Cloud Microphysics on the Development of
611 Trailing Stratiform Precipitation in a Simulated Squall Line: Comparison of One- and Two-Moment
612 Schemes, Mon. Weather Rev., 137, 991–1007, https://doi.org/10.1175/2008MWR2556.1, 2009.

613 Munassar, S., Monteil, G., Scholze, M., Karstens, U., Rödenbeck, C., Koch, F.-T., Totsche, K. U., and
614 Gerbig, C.: Why do inverse models disagree? A case study with two European CO 2 inversions,
615 Atmos. Chem. Phys., 23, 2813–2828, https://doi.org/10.5194/acp-23-2813-2023, 2023.

616 Nakanishi, M. and Niino, H.: An Improved Mellor–Yamada Level-3 Model with Condensation
617 Physics: Its Design and Verification, Boundary-Layer Meteorol., 112, 1–31,
618 https://doi.org/10.1023/B:BOUN.0000020164.04146.98, 2004.

619 Park, C., Gerbig, C., Newman, S., Ahmadov, R., Feng, S., Gurney, K. R., Carmichael, G. R., Park, S.-
620 Y., Lee, H.-W., Goulden, M., Stutz, J., Peischl, J., and Ryerson, T.: CO2 Transport, Variability, and
621 Budget over the Southern California Air Basin Using the High-Resolution WRF-VPRM Model during
622 the CalNex 2010 Campaign, J. Appl. Meteorol. Climatol., 57, 1337–1352,

https://doi.org/10.1175/JAMC-D-17-0358.1, 2018.

Patra, P. K., Takigawa, M., Watanabe, S., Chandra, N., Ishijima, K., and Yamashita, Y.: Improved Chemical Tracer Simulation by MIROC4.0-based Atmospheric Chemistry-Transport Model (MIROC4-ACTM), SOLA, 14, 91–96, https://doi.org/10.2151/sola.2018-016, 2018.

Pillai, D., Buchwitz, M., Gerbig, C., Koch, T., Reuter, M., Bovensmann, H., Marshall, J., and Burrows, J. P.: Tracking city CO2 emissions from space using a high-resolution inverse modelling approach: a case study for Berlin, Germany, Atmos. Chem. Phys., 16, 9591–9610, https://doi.org/10.5194/acp-16-9591-2016, 2016.

Pisso, I., Patra, P., Takigawa, M., Machida, T., Matsueda, H., and Sawa, Y.: Assessing Lagrangian inverse modelling of urban anthropogenic CO2 fluxes using in situ aircraft and ground-based measurements in the Tokyo area, Carbon Balance Manag., 14, 6, https://doi.org/10.1186/s13021-019-0118-8, 2019.

Steinkamp, K., Mikaloff Fletcher, S. E., Brailsford, G., Smale, D., Moore, S., Keller, E. D., Baisden, W. T., Mukai, H., and Stephens, B. B.: Atmospheric CO2 observations and models suggest strong carbon uptake by forests in New Zealand, Atmos. Chem. Phys., 17, 47–76, https://doi.org/10.5194/acp-17-47-2017, 2017.

Sugawara, H., Ishidoya, S., Terao, Y., Takane, Y., Kikegawa, Y., and Nakajima, K.: Anthropogenic CO2 Emissions Changes in an Urban Area of Tokyo, Japan, Due to the COVID-19 Pandemic: A Case Study During the State of Emergency in April–May 2020, Geophys. Res. Lett., 48, https://doi.org/10.1029/2021GL092600, 2021.

Tewari, M., Chen, F., Wang, W., Dudhia, J., LeMone, M., Mitchell, K., Ek, M., Gayno, G., Wegiel, J., and Cuenca, R.: Implementation and verification of the unified NOAH land surface model in the WRF model, 20th conference on weather analysis and forecasting/16th conference on numerical weather prediction, Am. Meteorol. Soc. Seattle, WA, US, 11–15, 2004.

Tohjima, Y., Patra, P. K., Niwa, Y., Mukai, H., Sasakawa, M., and Machida, T.: Detection of fossil-fuel CO2 plummet in China due to COVID-19 by observation at Hateruma, Sci. Rep., 10, 18688, https://doi.org/10.1038/s41598-020-75763-6, 2020.

Yamashita, Y., Takigawa, M., Goto, D., Yashiro, H., Satoh, M., Kanaya, Y., Taketani, F., and Miyakawa, T.: Effect of Model Resolution on Black Carbon Transport from Siberia to the Arctic Associated with the Well-Developed Low-Pressure Systems in September, J. Meteorol. Soc. Japan. Ser. II, 99, 2021–014, https://doi.org/10.2151/jmsj.2021-014, 2021.

Zhang, B., Cressie, N., and Wunch, D.: Inference for Errors-in-Variables Models in the Presence of Systematic Errors with an Application to a Satellite Remote Sensing Campaign, Technometrics, 61, 187–201, https://doi.org/10.1080/00401706.2018.1476268, 2019.

657

658

659